nature communications

Article https://doi.org/10.1038/s41467-024-53016-8

One-pot microfluidic fabrication of micro ceramic particles

Received: 2 January 2024

Accepted: 24 September 2024

Published online: 15 October 2024

Check for updates

Chenchen Zhou[1,2], Shuaishuai Liang[3], Bin Qi[3], Chenxu Liu[4] & Nam-Joon Cho[1,2]

In the quest for miniaturization across technical disciplines, microscale ceramic blocks emerge as pivotal components, with performance critically dependent on precise scales and intricate shapes. Sharp-edged ceramic microparticles, applied from micromachining to microelectronics, require innovative fabrication techniques for high-throughput production while maintaining structural complexity and mechanical integrity. This study introduces a "one-pot microfluidic fabrication" system incorporating two device fabrication strategies, "groove & tongue" and sliding assembling, achieving an unprecedented array of microparticles with diverse, complex shapes and refined precision, outperforming traditional methods in production rate and quality. Optimally designed sintering profiles based on derivative thermogravimetry enhance microparticles' shape retention and structural strength. Compression and scratch tests validate the superiority of microparticles, suggesting their practicability for diverse applications, such as precise micromachining, sophisticated microrobotics and delicate microsurgical tools. This advancement marks a shift in microscale manufacturing, offering a scalable solution to meet the demanding specifications of miniaturized technology components.

The evolution of microscale material fabrication is a defining trend in numerous industries, from electronics[1,2] to micro-robotics[3,4] and surgical instrument[5,6] manufacturing. The ability to process microparticles (MPs) with precision is increasingly crucial, with the choice of material being central to their function. Ceramics are in the spotlight for their exceptional properties—hardness, wear resistance, resilience to high temperatures and chemicals, coupled with low thermal conductivity. The utility of ceramic MPs is diverse, influenced by their shape and material composition[7–11]. A multitude of techniques have been explored for the creation of MPs[12,13]. Methods like micro-wire electrical discharge machining (μWEDM) and micro grinding offer contactless fabrication of MPs, yet their application is confined to conductive materials[12]. Alternative methods employing ion or laser beams can sculpt MPs from a broader range of materials with high fidelity[14,15], but such processes come at a steep cost. Mechanical machining has been engaged to produce shanked MPs, though achieving high precision remains elusive[16]. Projection micro stereolithography excels in crafting ultrafine microparts; however, it's predominantly suitable for UV-curable resins[17] and limited by low production rates. Micro injection molding (μIM), while capable of processing a diverse array of materials at increased production speeds, is hindered by its inherently batch-wise production flow, which impedes continuous manufacturing and thus limits throughput.

Microfluidic lithography has been utilized to fabricate diverse MPs with high monodispersity, precision, and throughput[18,19], which includes sharp-edged 3D anisotropic transparent[20,21] and spherical/bowl-shaped nontransparent MPs[22,23]. However, the UV light path distortion caused by reflection, scattering, and refraction of the dispersed nanoparticles (NPs) makes it almost impossible to obtain sharp-edged MPs through microfluidic lithography, let alone fabricating them with

[1]School of Materials Science and Engineering, Nanyang Technological University, Singapore 639798, Singapore. [2]Centre for Cross Economy, Nanyang Technological University, Singapore 637551, Singapore. [3]School of Mechanical Engineering, University of Science and Technology Beijing, Beijing 100083, P.R. China. [4]Department of Mechanical Engineering, Tsinghua University, Beijing 100084, P.R. China. e-mail: njcho@ntu.edu.sg

higher strength by increasing NP content. Therefore, a "one-pot microfluidic fabrication" (OPMF) system incorporating thermocuring modules is innovatively presented. The production rate of MP tools is improved by more than two orders of magnitude while maintaining the equivalent roughness, sharpness, size range and shape complexity as the microtools obtained through existing methods.

Owning to the strict precision requirements for microfluidic channel (MC) mold manufacturing and considerable difficulties in MC demolding, it remains challenging to create precise PDMS MCs with cross-sections that are not based on rectangles[24–26]. Drawing upon the ancient Chinese carpentry technique of the "mortise & tenon joint", the OPMF system introduces a precise "groove & tongue" assembling (GTA) strategy for various non-rectangular MCs fabrication, which offers a creative leap in shaping MPs by allowing for intricate and precise structures previously unattainable. Furthermore, the established practice in microfluidics often restricts the use of templating molds to produce MCs with uniform cross-sections[8,20,21,27], limiting their versatility. Inspired by another pearl of ancient wisdom, the "Chinese Tangram", our research transcends this boundary by pioneering a "sliding assembling" (SA) technique. This innovation enables the use of a singular mold to fabricate a variety of MCs, not only broadening the scope of potential MC and MP designs but also promoting a more efficient and eco-friendly manufacturing process.

To date, sharp-edged anisotropic MPs crafted through microfluidics have found their primary applications in cell manipulation[28], bioassays[29,30], anticounterfeiting[31–33] and so forth. However, their use as micro tools/parts has been hindered by challenges such as low material density, fragility and limitations with nontransparent materials[34]. Addressing these issues, our work enhances the density and strength of MPs by increasing the solid content and employing optimally designed sintering profiles. Moreover, we delve into the realm of nontransparent materials, such as Al_2O_3 and Si_3N_4, achieving MPs that exhibit the required durability and toughness to process substrates of various materials, including metals, plastics and wood. These advancements showcase the potential of these robust MPs to function as key components in micro-electromechanical systems (MEMS), micro-robots, and as precise instruments in micromachining and microsurgery, marking a progressive stride in microscale material fabrication.

Results and discussion

OPMF system for gear-shaped MP fabrication

OPMF system separates the acrylamide-based polymerization precursor into two parts based on characteristics of component reagents: bulk solution (BS) for the mixture of NP dispersion and prepolymers (acrylamide and N, N′-methylenebisacrylamide), curing solution (CS) for an aqueous mixture of ammonium persulfate and N, N, N′, N′-tetramethyl ethylenediamine that initiate and accelerate the polymerization. BS and CS remain stable individually but react promptly upon meeting each other. A microfluidic device is designed to be divided into three functional zones for precursor feeding, mixing and curing, respectively (Fig. 1a, Supplementary Fig. 1). A mixer, comprising a magnetic bead confined within the workspace by two fixed pillars, is magnetically driven to enhance convection between BS and CS. Mixed precursor uniformly fills MC before the curing zone ("A – A") and is gradually cured by the heat transferred from the peripherally wrapped copper sheet after entering the curing zone ("B – B"), where the crosslinking reaction occurs massively and forms a 3D netlike polymer structure. Oxygen diffuses through the PDMS wall and reacts with initiator species to form chain-terminating peroxide radicals[35], inhibiting polymerization reaction[36]. Oxygen concentration $C(O_2)$ increases with proximity to the MC wall[37]. Therefore, a thin lubricating layer forms, facilitating the smooth extrusion. Nevertheless, as the liquid ceramic precursor gradually transforms into solid microfiber green bodies, the abrasion at the MC curing zone caused by the contact of crosslinked polymer containing ceramic NPs becomes increasingly nonnegligible[38,39], which needs to be further investigated in the following studies.

Inspired by the ancient Chinese timber structure "mortise & tenon joint", GTA is presented to precisely fabricate MCs with both rectangular and non-rectangular cross-sections. Precisely coordinated grooves and tongues control the relative positions of MC substrate pieces and ensure the precise alignment of MC inner walls. GTA can be utilized to fabricate MCs possessing multiple separated pieces, increasing MPs' shape complexity. Here, a gear-shaped MC with ten teeth is created (Fig. 1b, Supplementary Figs. 2–4). Each separated MC piece features an intact contour of a gear tooth, encompassing contour lines for one top land, one bottom land, two faces, two flanks and two fillets. A tongue and groove are set on the center of two opposite oblique side walls. MC is secured after assembling. The gradually enlarged views of MC show good cooperation between grooves and tongues, as well as a clear gear-shaped cross-section.

NPs with three materials, SiO_2, Al_2O_3 and Si_3N_4, are respectively integrated to form stable BSs (Supplementary Figs. 5, 6). SiO_2 – BS is about half transparent on average across the UVA wavelength range (315 – 400 nm); nevertheless, Al_2O_3/Si_3N_4 – BSs show zero light transmittance in the 250 – 800 nm range due to light scattering, reflection and refraction caused by the NPs (Fig. 1c). Precursors made from such opaque BSs can only be solidified into desire-shaped MPs through high-intensity/long-time UV light curing within the templates such as droplets[22,23], concave molds[7] and so forth. Here, the OPMF system allows us to create sharp-edged MPs using both transparent and nontransparent precursors.

The average viscosities of three shear-thinning BSs are 14.7, 115.7 and 571.1 mPa·s, respectively (Fig. 1d, Supplementary Table 1, Supplementary Figs. 7, 8), indicating the OPMF system is well-suited for BSs with a viscosity ranging from tens to hundreds of mPa·s. BS and CS contact and mix at the start of the mixing zone, where storage modulus G′ dramatically increases and exceeds the loss modulus G″ of the precursor (Fig. 1e), indicating the fluid-gel transition occurs and crosslinked polyacrylamide (PAM) is formed. As temperature increases, G′ and G″ increase and gradually stabilize at ~10^5 Pa after reaching ~60 °C, which is also tested as the optimal heating temperature for OPMF system to fabricate Al_2O_3, SiO_2, and Si_3N_4 microfiber green bodies at the optimized flow rates 12, 18, and 10 µL/min, respectively (Supplementary Figs. 9, 10).

Microfiber green bodies are subsequently cut into intact MPs with homogenous cross-sections (Fig. 1f, Supplementary Figs. 9–11). For example, distributions of outer diameter D_o, root diameter D_r and cross-section area a_g of the gear-shaped MPs demonstrate their high homogeneity with coefficients of variation calculated as 2.09%, 2.17% and 3.72%, respectively (Fig. 1g). The OPMF system exhibits higher production rates compared to traditional methods (Supplementary Tables 5–8), positioning it as a promising technology for the mass production of micro torque-transmitting components in MEMS and microrobots.

GTA and SA for diverse MPs fabrication

GTA aforementioned is further exemplified by introducing more cross-section shapes, including regular triangle, hexagon, isosceles triangle and trapezoid (Fig. 2a). MPs incorporated with SiO_2, Al_2O_3 and Si_3N_4 NPs respectively show transparent, opaque white and brown looks under the microscope. Sharp corners, clear edges, and great homogeneity of MPs verify the superiority of GTA (Fig. 2b, Supplementary Fig. 12). SiO_2, Al_2O_3 and Si_3N_4 MP green bodies shrink about 35%, 14% and 16% after drying. Oxygen inhibition is prevalent in numerous free-radical polymerization reactions, rendering our OPMF system suitable for producing MPs with more diverse materials. However, this one-to-one correspondence of GTA between mold and MC limits the mold's shape-creation capacity. SA, inspired by another ancient Chinese

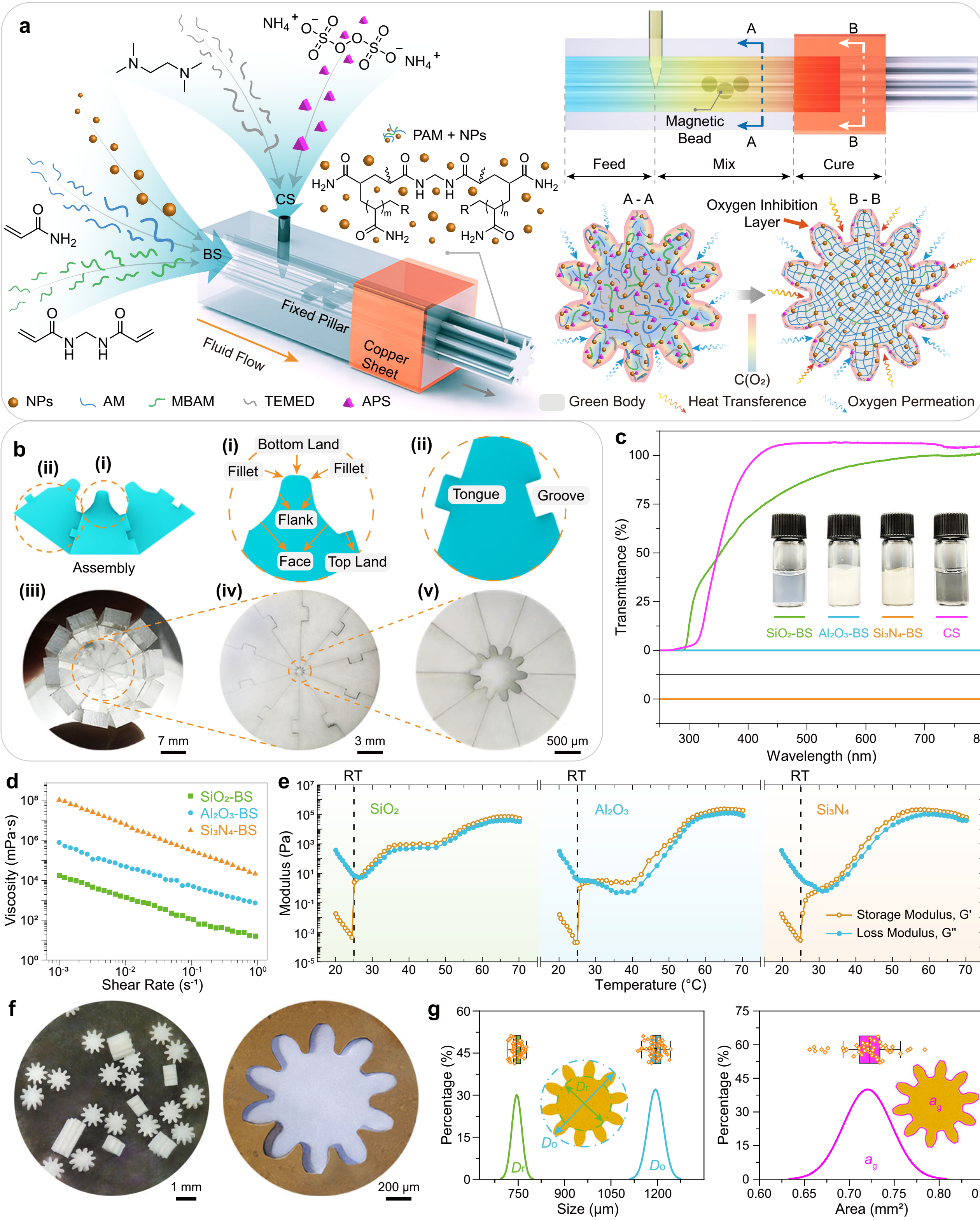

Fig. 1 | Fabrication of gear-shaped microparticles (MPs) by "one-pot microfluidic fabrication" (OPMF) system. a Schematic illustrations for the OPMF system and synthesizing mechanism. An anqueous bulk solution (BS), composed of nanoparticles (NPs), acrylamide (AM), and N, N′-methylenebisacrylamide (MBAM), is injected into microfluidic device along with the curing solution (CS) which is composed of N, N, N′, N′-tetramethyl ethylenediamine (TEMED) and ammonium persulfate (APS). After online mixing and in-situ polymerization, a compound made out of polyacrylamide (PAM) and NPs is fabricated. **b** "Groove & tongue" assembling for gear-shaped microfluidic channel (MC) fabrication inspired by the ancient Chinese "mortise & tenon joint" timber structure. **c** UV-vis spectra and images of BSs and CS. **d** Viscosity characterization of three BSs determined by shear rate. **e** Modulus transformation imitation of the precursor inside MCs during synthesizing. **f** Optical images of the obtained gear-shaped MPs. **g** Distribution curves and statistical analysis for outside diameter (D_o), root diameter (D_r) and cross-section area (a_g) of the obtained gear-shaped MPs with the population number 50. Source data are provided as a Source Data file.

https://doi.org/10.1038/s41467-024-53016-8

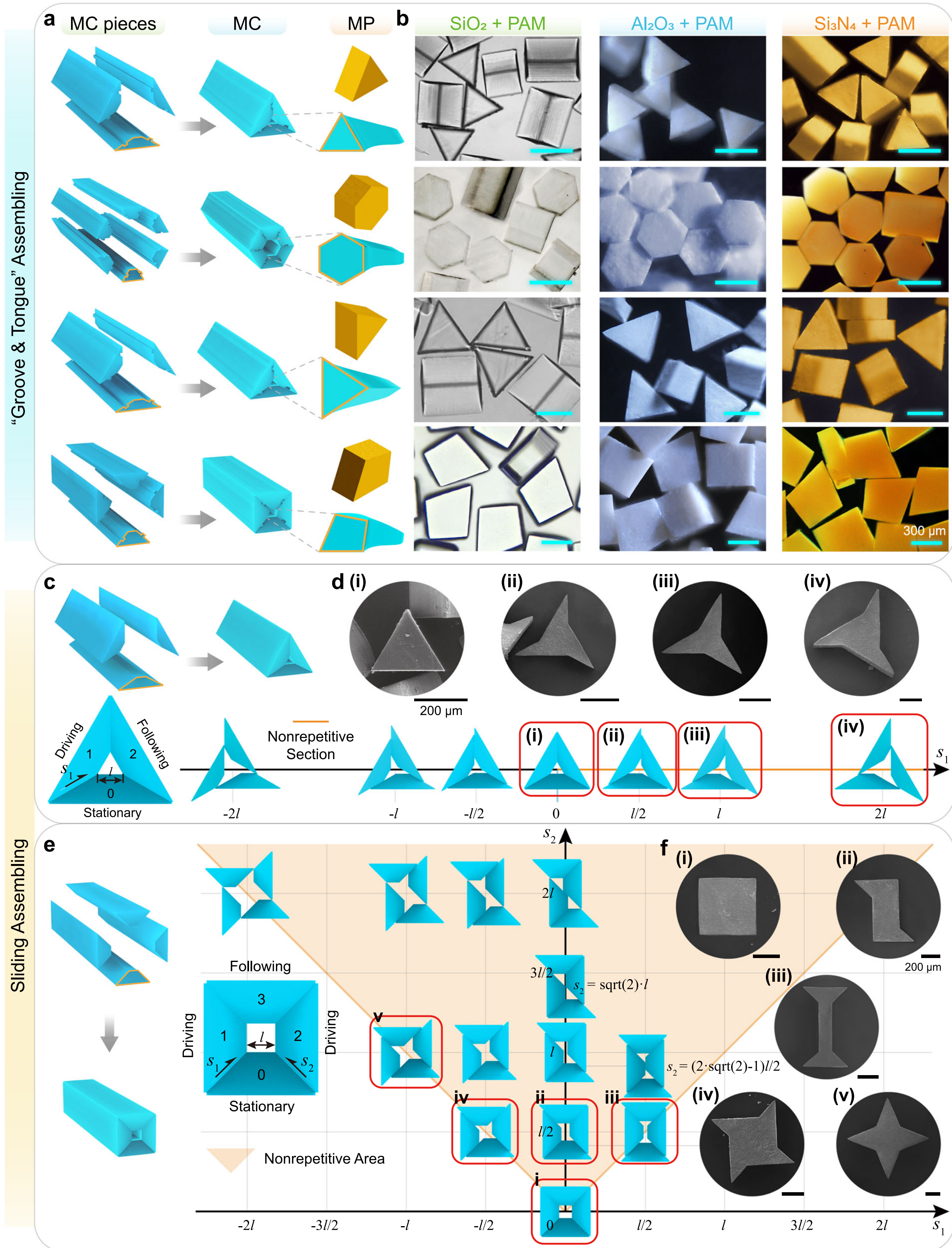

Fig. 2 | "Groove & tongue" and sliding assembling microfluidic channel (MC) fabrication strategies for preparing microparticle (MP) green bodies with various shapes and materials. a Schematic illustrations for "groove & tongue" assembling with MC cross-sections including regular triangle, hexagon, isosceles triangle and trapezoid. **b** Optical micrographs of the corresponding-shaped MP green bodies containing nanoparticles (NPs, including SiO_2, Al_2O_3 and Si_3N_4) and binding polymer polyacrylamide (PAM). **c** Demonstrative schematic illustrations of the triangular MC cross-section (side length *l*) transformation by tuning the sliding distance s_1. **d** Scanning electron microscope (SEM) images of i, triangular and ii-iv, star-shaped MP green bodies. **e** Demonstrative schematic illustrations of the square MC cross-section (side length *l*) transformation through tuning the sliding distances s_1 and s_2. **f** SEM images of the MP green bodies with shapes resembling i, square, ii, "Z", iii, "I" and iv, v, quadrangular stars.

wisdom, "Tangram", is presented pertinently to overcome this limitation by allowing adjacent MC pieces to slide at the smooth interface in between, leading to the generation of MCs with various cross-sections and sharp cutting edges (Fig. 2c, Supplementary Fig. 13). Polycarbonate (PC) clamps were attached peripherally around the MC after sliding to a specific configuration, immobilizing the segmental MC pieces and pressing them sealed (Supplementary Fig. 14). The shape-creation capacity of MCs obtained using one mold is infinite due to the variation of sliding distance (s). Assuming the number of MC pieces is N, the degree of sliding freedom (DSF) for MC assembling is N-2. Immobilizing one of the separated pieces (defined as piece 0), the number of pieces that can be moved flexibly under the driving force is N-2, while the remaining one piece is a follower.

There is only one driving piece for triangular MC. As s_1 increases from 0 to infinity, the cross-section of MC transforms from a regular triangle ($s_1 = 0$) to a three-pointed star ($s_1 = l$), then to a regular triangle with three negligible triangular barbs extended from each corner ($s_1 = \infty$), where l is defined as the side length of the cross-section (Fig. 2c, d). When piece 1 is driven along the negative direction, the obtained MC cross-section shapes are mirror-symmetrical to those driven along the positive direction. For rectangular MC, pieces 1 and 2 are both defined as driving pieces. The MC cross-section transforms as sliding distances s_1 and s_2 vary (Fig. 2e). MCs with numerous cross-sections can be obtained (Supplementary Fig. 15), indicating a further enlarged shape-creation capacity of the mold. The cross-section shapes are mirror-symmetrical about the line $y = x$. Additionally, the cross-section shapes on one side of the line $y = -x$ can be transformed into the shapes on the other side by rotating 90° about their centroids. Cross-section shapes at some special points are selected to manifest the shape variation trend as s_1 and s_2 vary, among which square, "Z/I" shapes and four-pointed stars are chosen to be experimentally fabricated (Fig. 2f).

Characterization of MPs before, during and after sintering

The compositions and structures of the obtained MP green bodies are verified by Fourier transform infrared (FTIR, Supplementary Fig. 16) and X-ray photoelectron spectroscopy (XPS, Supplementary Fig. 17). The compositional elements of each sample are well-mixed and distributed uniformly (Supplementary Figs. 18, 19), indicating the homogeneous mixing of our OPMF system. MP green bodies are then rebound and densified through high-temperature sintering (Fig. 3a, b, c). They dehydrate before ~113 °C with slight mass loss due to prior 24-h air drying. Then, polymer PAM in four samples mainly goes through two endothermic processes, glass transition and melting, subsequently at 113–345 °C, during which the polymer transforms from a stiff "glassy" state to a soft "rubbery" state[40,41], then to a liquid state. As the temperature keeps increasing, PAM decomposes into multiple smaller molecules, H_2O and gases[42] before 480 °C and is finally combusted under the synthetic effect of heat and oxygen at 480–708 °C. Sample's weight decreases significantly, and plenty of heat is released during decomposition and combustion. Notably, there is a prominent weight increase and a conspicuous exothermic peak for the Si_3N_4 sample at 1173–1327 °C due to oxidation of the sample surface with the main chemical reaction described as follows[43,44].

$$Si_3N_4(s) + 3O_2(g) = 3SiO_2(s) + 2N_2(g) \quad (1)$$

Weight loss and heat flow of the samples vary with their polymer content. Due to the lower PAM content, SiO_2, Al_2O_3 and Si_3N_4 green bodies have relatively lower weight/heat change during debinding. To preserve MPs from cracking caused by drastic mass/volume change and ensure the final sintering quality, the sintering profiles for different MPs are designed pertinently by derivative thermogravimetry (DTG) analysis and referring to the previous studies that are widely recognized (Supplementary Fig. 20, Supplementary Table 2). After sintered, SiO_2, Al_2O_3 and Si_3N_4 samples undergo isotropic linear shrinkages about 25.6%, 19%, and 5.3%, respectively (Supplementary Fig. 21), while their monodispersity, shape retentivity, and shape fidelity remain great (Fig. 3d, e, i, k, Supplementary Fig. 22). The densities of three samples reach 2.20, 3.93, and 3.01 g/cm^3 respectively, indicating their great potential for industrial applications (Supplementary Table 3 and Supplementary Fig. 23).

Densely packaged grains ranging from 1 to 5 µm (Fig. 3f) make a roughness (R_a) ~ 0.255 µm of the Al_2O_3 MP surface (Fig. 3m, p). The distance (0.255 nm) between adjacent lattice fringes is in good accordance with the Al_2O_3 (1 0 4) crystal face at $2\theta = 35.136°$ (Fig. 3g, h). Hexagonal corundum (PDF#10-0173, Fig. 3q), a high-temperature polymorph of Al_2O_3, is obtained. SiO_2 MP comprising nanosized partially molten grains has a dense surface with a R_a ~ 0.391 µm (Fig. 3j, n). Its crystal structure corresponds with cristobalite (PDF#39-1425, Fig. 3r), while Si_3N_4 MP has multiple crystal structures (Fig. 3s), including cristobalite (PDF#89-3607), β-Si_3N_4 (PDF#33-1160) and Si_2N_2O (PDF#83-2149). Cristobalite is formed after the oxidation of Si_3N_4 NPs through Reaction (1). Sintering additives Y_2O_3 and Al_2O_3 react with SiO_2 and form a silicate liquid phase Y-Si-Al-O-N, promoting the sintering process[45,46]. α-Si_3N_4 grains are transformed into β-Si_3N_4 grains through a solution-precipitation process in the presence of the liquid phase[47]. The rod-like elongated β-Si_3N_4 grains (Fig. 3l) act as whisker-reinforcing agents in the matrix, strengthening the composite[48,49]. Si_2N_2O is formed from the reaction of SiO_2 and Si_3N_4 in the presence of a liquid phase, with the main chemical reaction described as follows[50,51].

$$SiO_2(s) + Si_3N_4(s) = 2Si_2N_2O(s) \quad (2)$$

Besides, the liquid phase finds its equilibrium at grain boundaries, making the MPs of high density and great smoothness[46]. As a result, the R_a of some localized surface regions is as low as ~0.249 µm, while it increases to 0.754 µm for an enlarged surface region due to the bumpy topography (Fig. 3o).

Performance assessment of MPs and OPMF system

Prismatic ceramic MPs possessing square, isosceles triangular and star-shaped cross-sections are selected as model MPs obtained from GTA and SA MCs to test their mechanical strength and toughness. Square MPs are designated P0, triangular and star-shaped MPs with two postures (standing and lying) are designated P1 – 4, respectively (Fig. 4a). For MPs with the same shape and posture, Si_3N_4 MPs have the highest maximum force (F_{max}) and energy absorption (E_a), while SiO_2 MPs have the lowest. For example, sintered SiO_2, Al_2O_3, and Si_3N_4 cubes can withstand F_{max} of about 12.8, 22.3, and 36.2 N and absorb compressive energy of about 0.39, 0.98, and 1.45 mJ, respectively (Fig. 4b–d). These MPs have the moderately ranked strength among the materials that can be potentially fabricated by the traditional methods (Supplementary Fig. 24). The force–displacement curves vary prominently with the structures of MPs (Fig. 4e–g). Compared with P1, P2 has shorter displacement and lower F_{max} owing to the high intensity of the pressure exerted on its top edge. P4 withstands larger pressing displacement and higher F_{max} than P3. The destructions of four lateral sharp edges of P4 absorb and dissipate more compressive energy, and lead to several sharp force drop-offs. Meanwhile, due to the increased number of pressure-bearing edges, P4 also possesses larger F_{max} and E_a than P2. Besides, the bending tests combined with Weibull analysis demonstrate the homogeneity in flexural strength σ, with average values calculated as 71.8, 184.5 and 197.3 MPa for the obtained SiO_2, Al_2O_3 and Si_3N_4 MPs (Supplementary Fig. 25, Supplementary Table 4).

The practical application performance of the rigid MPs is tested through scratch tests. Six types of MPs, including triangular/star-shaped Al_2O_3 (T/S-Al_2O_3), SiO_2 (T/S-SiO_2), Si_3N_4 (T/S-Si_3N_4) MPs, are

 https://doi.org/10.1038/s41467-024-53016-8

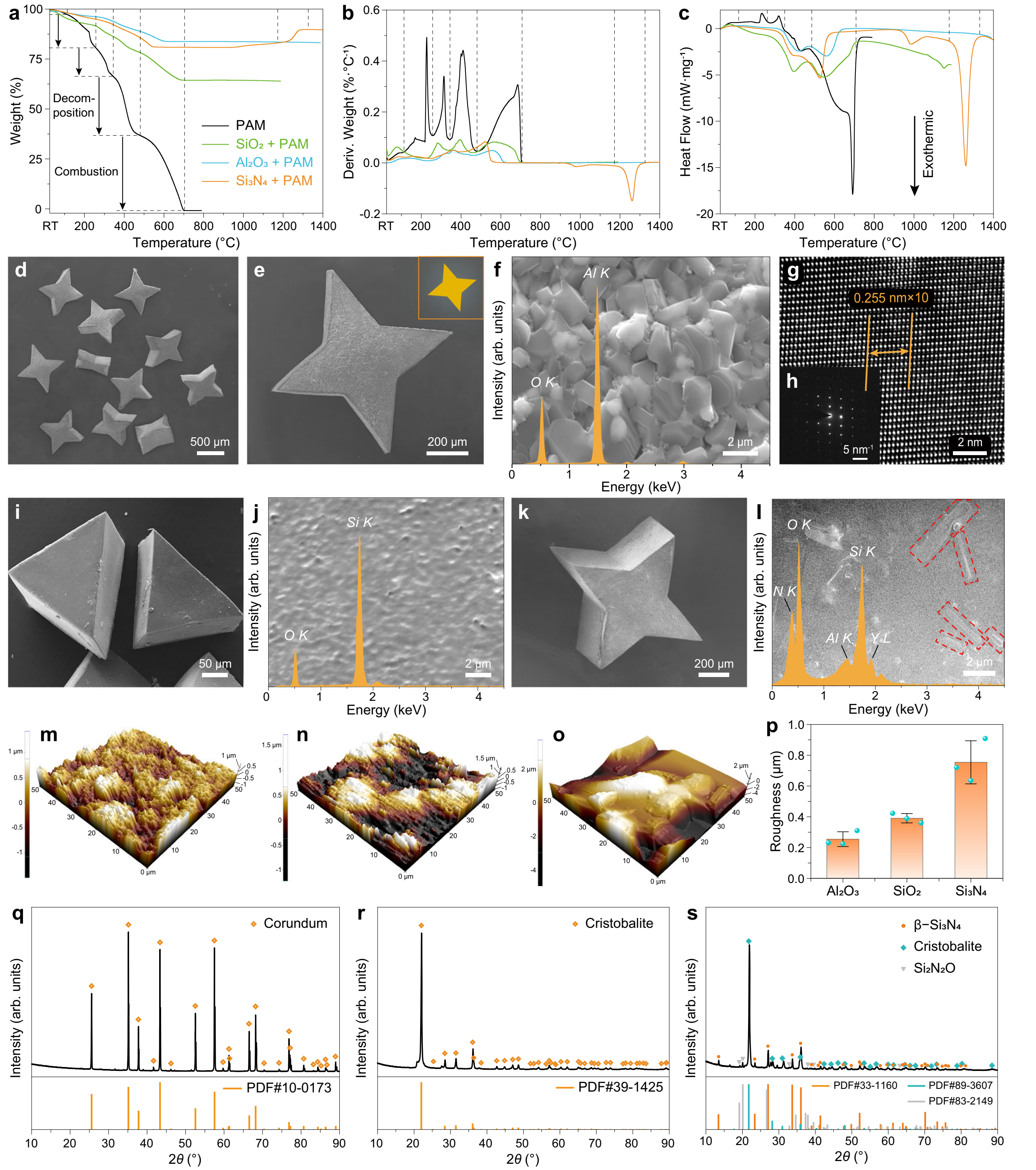

Fig. 3 | Characterization of microparticles (MPs) before, during and after sintering. a Thermogravimetric analysis, **b** Derivative of weight loss and (**c**) Differential scanning calorimetry characterizations of samples during sintering. The samples include synthesized polyacrylamide (PAM) and compounds made of PAM and three different nanoparticles. **d** Scanning electron microscope (SEM) image of several star-shaped Al_2O_3 MPs. **e** SEM image of a single star-shaped Al_2O_3 MP consistent with the model's shape at the upper right corner. **f** High-magnification SEM image of the crystalline grains on Al_2O_3 MP's surface with energy-dispersive X-ray (EDX) spectra floating above. **g** Transmission electron microscope (TEM) image of the crystalline lattice fringes of Al_2O_3 MPs and its converted (**h**) diffraction spots. **i**, SEM image of the isosceles triangular SiO_2 MPs. **j** High-magnification SEM image of SiO_2 MP's surface with EDX spectra floating above. **k** SEM image of a star-shaped Si_3N_4 MP. **l**, High-magnification SEM image of Si_3N_4 MP's surface with EDX spectra floating above. Atomic force microscope (AFM) images showing the surface topographies of (**m**, Al_2O_3, **n**, SiO_2 and **o**) Si_3N_4 MPs. **p** Surface roughness of three sintered MPs, data are represented as mean values ± s.d. from three samples. X-ray diffraction (XRD) patterns of (**q**, Al_2O_3, **r**) SiO_2 and (**s**) Si_3N_4 MPs. Source data are provided as a Source Data file.

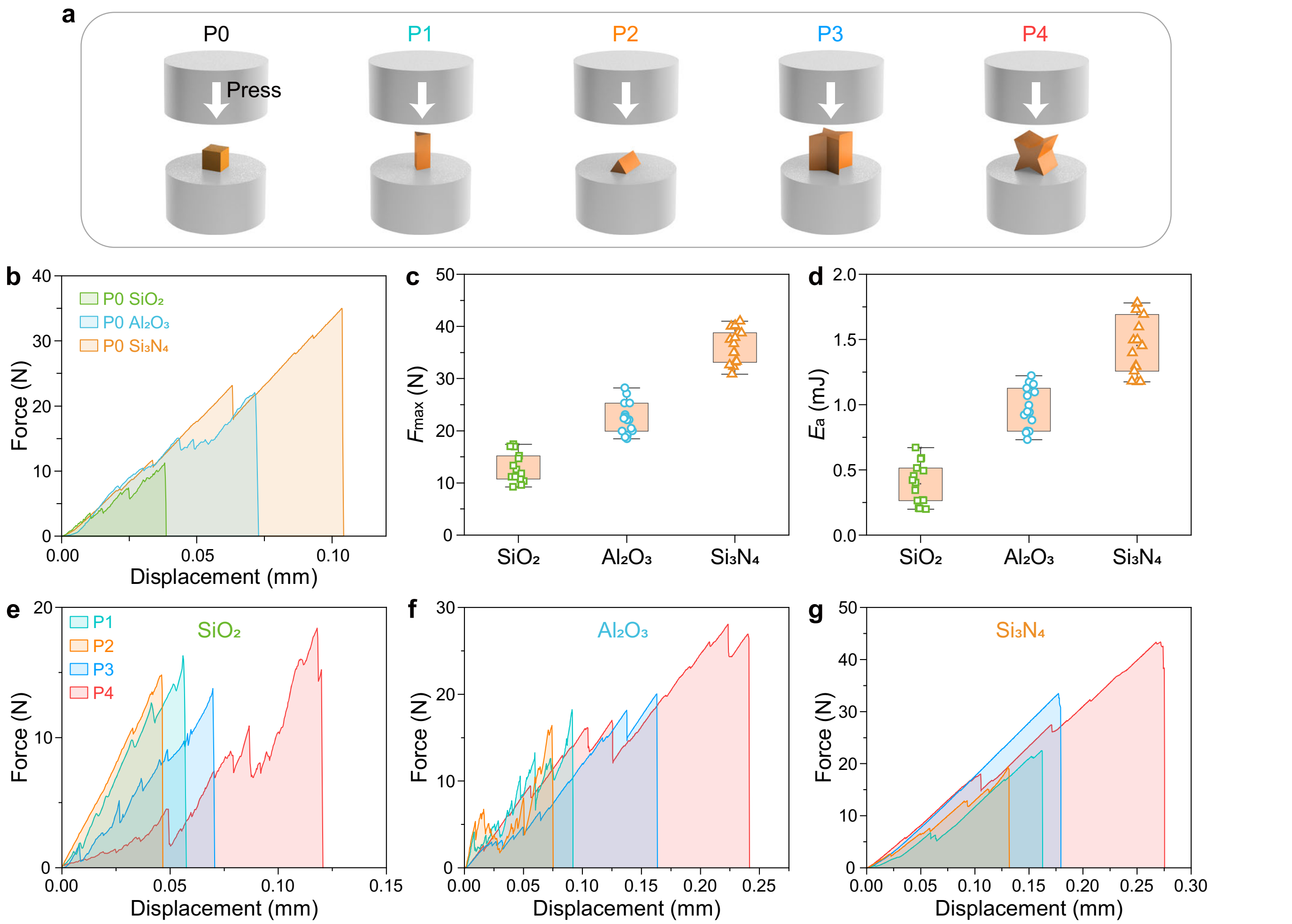

Fig. 4 | Compression tests for sintered microparticles (MPs) with cross-sections including square, isosceles triangle and star-shape. a Schematic illustrations of compression tests for sintered MPs with various shapes and postures, P0 for square MPs, P1 for triangular standing MPs, P2 for triangular lying MPs, P3 for star-shaped standing MPs and P4 for star-shaped lying MPs. **b** Force−displacement curves of P0 with SiO_2, Al_2O_3 and Si_3N_4 materials. **c** The maximum force (F_{max}) and **d** energy absorption (E_a) of P0 MPs during the compression process before failure, data are represented as mean values ± s.d. from 15 samples. **e**–**g** Force−displacement curves of P1, P2, P3 and P4 with SiO_2, Al_2O_3 and Si_3N_4 materials. Source data are provided as a Source Data file.

used to scratch the substrates made of five materials including T2 copper (Cu), 7075 aluminum alloy (Al), polystyrene (PS), polymethyl methacrylate (PMMA) and wood (Fig. 5a). The MPs are positioned at a slant angle of 70° intersecting the substrates with their cusps. Star-shaped MPs have lower maximum force withstood by their cusps before failure (CF_{max}) than triangular ones (Fig. 5b) because their cutting cusps are sharper and relatively easier to break. SiO_2 MPs have the lowest CF_{max}, while Si_3N_4 MPs possess the highest, consistent with the ranking order of compressive strength. To prevent MP cusps from being broken during scratching, we conservatively set the forces applied to T-SiO_2/Al_2O_3/Si_3N_4 and S-SiO_2/Al_2O_3/Si_3N_4 MPs as 1.5, 9, 13, 1, 6 and 9 N, respectively. Z-stack scanning is applied to reconstruct 3D shapes of various scratches and measure their width (w), height (h) and volume loss. The scratches on metal (Cu, Al) and polymeric plastic (PS, PMMA) substrates have clear traces and distinct profiles, while the scratches obtained on wood substrates are somewhat out of shape due to the interference of the intertwined component wood fibers (Fig. 5d, e, f, Supplementary Figs. 26–28). After analyzing w, h and volume loss of 477 µm-long scratches in the images, substrate materials can be ranked as Al > Cu > PMMA > PS > wood based on their subtractive manufacturing difficulties, which is positively correlated with the hardness ranking of substrate materials (Fig. 5c). It's evident that Si_3N_4 MP tools are capable of removing more material than Al_2O_3 ones, while SiO_2 MP tools remove the least (Fig. 5g). These scratch tests demonstrate the practicability of using ceramic MP tools obtained through our work in micromachining fields.

The MP tools obtained through the OPMF system are compared with the microtools fabricated by other reported methods, including µWEDM, µIM, micro grinding, focused ion beam and femtosecond pulsed laser machining (Supplementary Tables 5–8). The edge number of the cross-section (N) is positively correlated with the shape complexity of the microtools. Limited by the machining precision, improving shape complexity becomes more difficult as microtools' size decreases. The circumcircle diameter (D_c) of the cross-section is used to describe the microtool's size universally (Fig. 6a). Inferred from the statistical results of N and D_c, the MP tools obtained in this study exhibit a broad size distribution, spanning across the size ranges of other methods, while maintaining equivalent shape complexity (Fig. 6b). In terms of the same machining methods, the shape fidelity of the microtool becomes more difficult to control as the size decreases. Here, the ratio between edge radius (R) and $D_c/2$ is used to evaluate the shape fidelity, where R is one of the most critical parameters for tools design. R of T-Al_2O_3 and S-Al_2O_3 MPs are representatively measured as 4.78 and 1.32 µm (Supplementary Fig. 22), and the corresponding $2R/D_c$ are calculated as 0.02529 and 0.00295, respectively, which are comparable with $2R/D_c$ from other methods

 https://doi.org/10.1038/s41467-024-53016-8

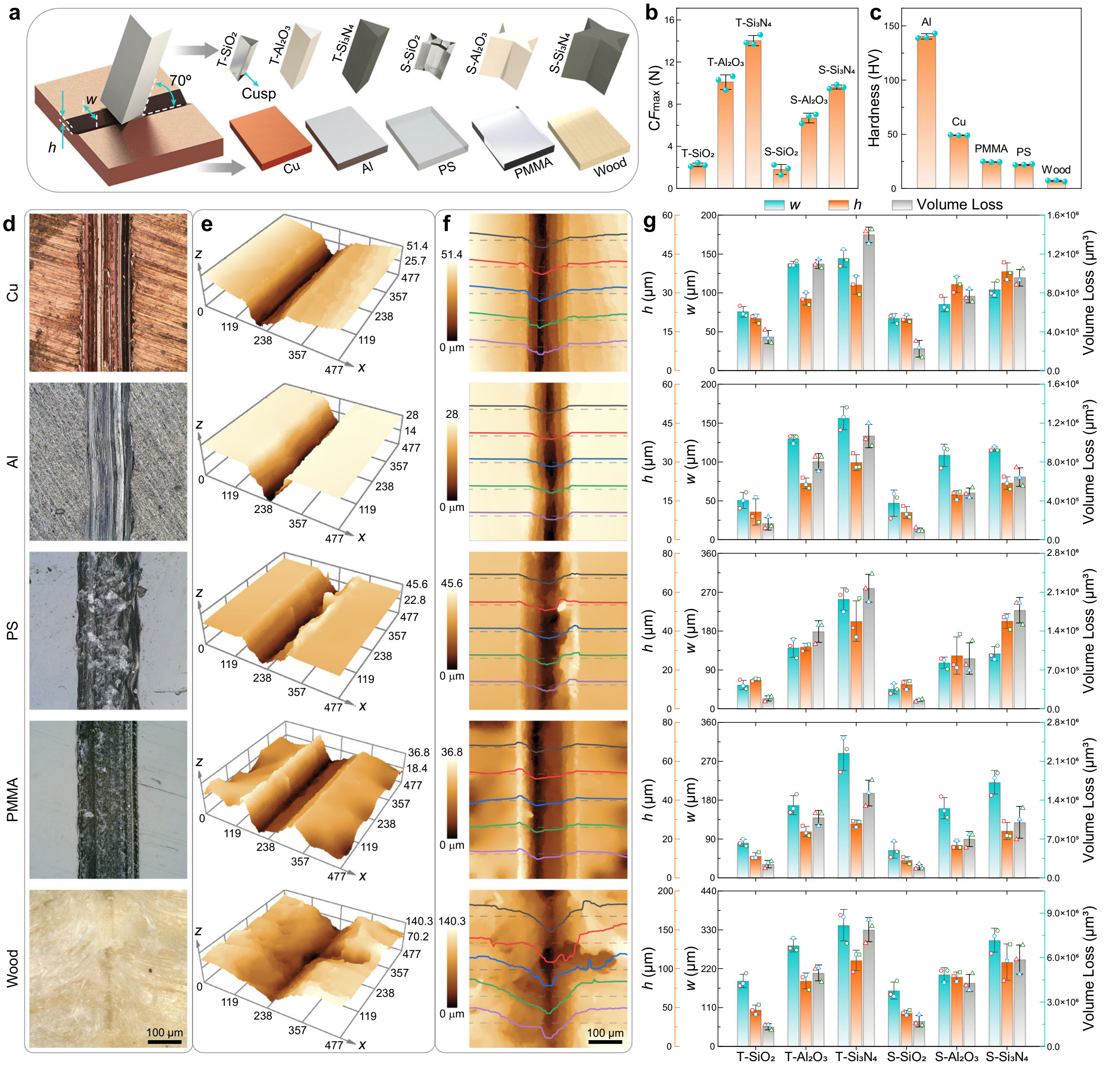

Fig. 5 | Scratch tests for isosceles triangular and star-shaped ceramic microparticles (MPs) with SiO_2, Al_2O_3 and Si_3N_4 materials. **a** Schematic illustrations of scratch tests using various MPs and multiple substrates including T2 copper (Cu), 7075 aluminum alloy (Al), polystyrene (PS), polymethyl methacrylate (PMMA) and wood. **b** Summary of the maximum forces for different MPs' cusps to withstand (CF_{max}) before failure, data are represented as mean values ± s.d. from three samples. **c** Hardness characterization for various substrates, data are represented as mean values ± s.d. from three samples. **d** Optical images and **e** 3D topographical maps of different scratches by Al_2O_3 MPs. **f** 2D cloud maps of scratches by Al_2O_3 MPs with cross-sectional profiles floating above. **g** Summary of width (w), depth (h) and volume loss of different scratches using different MPs and substrates, data are represented as mean values ± s.d. from three samples. Source data are provided as a Source Data file.

(Fig. 6c). Last and most importantly, R_a of microtools tends to be positively correlated with the processing rate in terms of the same method. This work is capable of increasing the processing rate by two orders of magnitude while keeping R_a below 1 μm, which is comparable with R_a obtained by other methods (Fig. 6d). In addition, the simple and efficient device design makes the OPMF especially cost-effective than other methods, which rely on bulky and expensive machines (Supplementary Fig. 29).

In summary, we present an OPMF system to fabricate various sharp-edged MPs with materials, including transparent SiO_2 and non-transparent Al_2O_3 and Si_3N_4. Besides, two types of MC designs inspired by ancient Chinese wisdom, including GTA and SA, are invented to increase the MCs' shape complexity, precision and diversity. Compared with existing methods for microtools fabrication, the production rate of our methods is improved by more than two orders of magnitude while keeping the equivalent MP shape complexity, diversity, size range, corner sharpness and surface roughness. By increasing the solid content and adopting optimally designed sintering procedures, the obtained MPs are endowed with great density, strength and toughness, being able to scratch the substrates made of various materials, including metals, plastics and wood. The obtained MPs show groundbreaking prospects for practical use as microtools in micromachining and microsurgery, as well as functional microcomponents in microrobots, MEMS, microelectronics and so forth.

https://doi.org/10.1038/s41467-024-53016-8

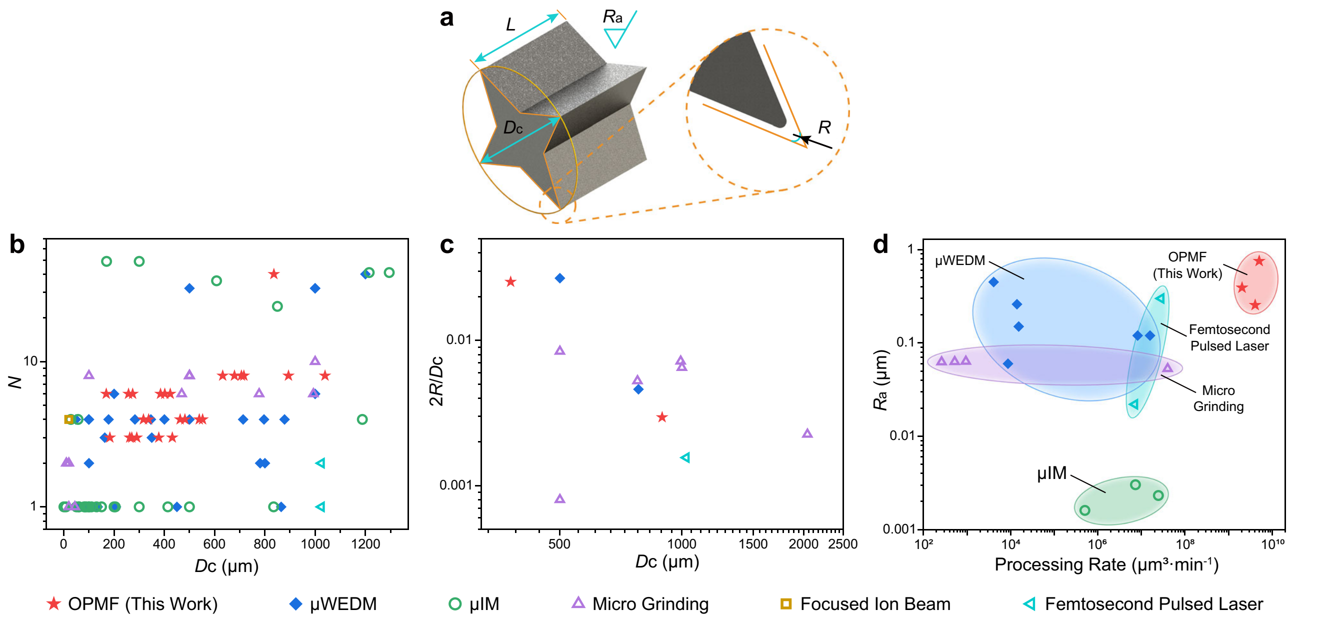

Fig. 6 | Comparisons of microparticles (MPs) obtained in this work with microtools reported by other works. a Schematic illustrations of critical parameters of microtools, including circumcircle diameter (D_c), edge radius (R), roughness (R_a) and length (L). Ashby plots of microtools in terms of (**b**) edge number (N) versus D_c, (**c**, $2R/D_c$ versus D_c and **d**) R_a versus processing rate. The references are listed in Supplementary Table 1. Source data are provided as a Source Data file.

Methods

Fabrication of microfluidic device

The metal molds made of stainless steel were fabricated by micro-wire electrical discharge machining using a machine tool (Shenzhen Wanqi CNC Equipment CO., Ltd.; DK7735). SYLGARD® 184 Silicone Elastomer Kit (Dow Corning) was used to fabricate PDMS reverse mold and MC substrate. A weight ratio of 5: 1 between the base fluid and the cross-linking oligomer was adopted to prepare the PDMS prepolymer. The prepolymer was stirred, degassed, and poured into the metal mold. The filled mold was also degassed and then heated in the oven at 65 °C for 1.5 h. After solidified, the PDMS reverse mold was demolded. Trichloro(octadecyl)silane (OTS, Sigma-Aldrich) was coated on the surface of the reverse mold as the releasing agent. PDMS prepolymer was poured into the reverse mold, degassed, and then heated at 65 °C for 45 min. The obtained semi-solidified MC substrate was demolded, and divided into several separated pieces, which were then assembled in a specific manner to form a closed MC. PC clamps were applied peripherally to secure the MC with a certain pressure (Supplementary Fig. 14). The cross-section shapes of the MC were tailored by adjusting the relative positions between the MC pieces and PC clamps. After being heated for another 45 min, the assembled fully cured MCs were trimmed to possess a square outer contour with a side length of 5 mm (Supplementary Fig. 4). A metal needle (60 μm in inner diameter) was used to punch holes through the side wall of the MC. A flat-ended metal needle (160 μm in inner diameter) was inserted into the center of the MC through the punched hole. A copper sheet (50 μm in thickness, 5 mm in width) was wrapped peripherally around the exit of MC. A magnetic bead (300 μm in diameter) was placed inside the MC with two steel rods (230 μm in diameter) confining its workspace (Supplementary Fig. 1).

Materials and reagents

The solution for synthesizing MP green bodies was divided into BS and CS. BS was prepared by mixing acrylamide (AM, Sinopharm Chemical Reagent Co., Ltd.; AR), N, N′-methylenebisacrylamide (MBAM, Coolaber Science and Technology Co., Ltd.; purity > 99.9%) and NP dispersions. We chose the commercially available colloidal silica (~30 nm NP average size, 27 vol% suspensions in H_2O, LUDOX CL-X, Sigma-Aldrich) as the SiO_2 NP dispersion[8,21,52]. Al_2O_3 NP dispersion was prepared by ball-milling the mixture containing α-Al_2O_3 ceramic powder (Almatis Co., Ltd.; 1 μm, purity ≥ 99.99 wt%), deionized (DI) water and triammonium citrate (TAC, Sinopharm Chemical Reagent Co., Ltd.; AR) at 450 rpm for 24 h in a planetary ball mill (Focucy, F-P2000). Zirconia milling balls with three different diameters (i.e., 3, 5, 10 mm) were added into each 100-mL zirconia jar at a ratio of 1:1:1 by weight. The balls to powder weight ratio is 2:1. After milled, Al_2O_3 NPs have an average diameter about 313 nm with a narrow size distribution (Supplementary Fig. 6). The volume ratio between the ceramic powder and the DI water was 1: 1, TAC was added at 1 wt% based on the powder[53–55]. 45 vol% α-Si_3N_4 ceramic powder (Shanghai Zhiliyejin Co., Ltd.; 1 μm, purity ≥ 99.9 wt%) with the addition of 5 vol% Y_2O_3 (Shanghai Macklin Biochemical Co., Ltd.; 1 μm, 99.99% metals basis) and 2.1 vol% α-Al_2O_3 (Almatis Co., Ltd.; 1 μm, purity ≥ 99.99 wt%) was suspended in DI water[56–58]. Tetramethylammonium hydroxide solution (TMAH, Shanghai Aladdin Biochemical Technology Co., Ltd.; 10 wt% in H_2O) was added at 6 vol% based on Si_3N_4 powder[57,59,60]. Si_3N_4 NP dispersion was obtained after ball-milling the mixture at 450 rpm for 24 h. AM was added to the above NP dispersions at 20% (w/v), and MBAM was added at 16.7 wt% based on AM. The CS of the system was the mixed aqueous solution comprised of the initiator ammonium persulfate (APS, Coolaber Science and Technology Co., Ltd.; purity ≥ 98%) and the catalyst N, N, N′, N′-tetramethyl ethylenediamine (TEMED, Shanghai Macklin Biochemical Co., Ltd.; purity ≥ 99%). The concentrations of APS and TEMED were 8.4 wt% and 4.5 vol%, respectively, based on CS. The washing solution was prepared by adding APS to DI water at 3 wt%. The aqueous aging solution was prepared by adding 3 wt% APS and 0.2 vol% TEMED.

MP green bodies fabrication

BS and CS were respectively injected into the microfluidic device with a flow rate ratio of 5: 1 by syringes (TERUMO®SYRINGE) using Teflon tubes (Anzijie Trade Co., Ltd.). Syringe pumps (LongerPump® LSP01-3A) were used to drive the fluids. The temperature of the copper sheet was controlled at 60 °C by a heating system consisting of a ceramic heating plate (XH-RP4040, 12W, Jiangsu Xinghe Electron Technology Co., Ltd), temperature sensor (XH-T112) and temperature controller (XH-W2030). The copper sheet transferred heat into the MC evenly. The magnetic bead was driven by a magnetic stirrer (DLAB, MS-H280-Pro) placed under the MC. Green microfibers were produced and collected at the exit of the MC. A blade (Gillette, double edge super stainless) polished by abrasive paper (Starcke, ST 1000, 3000, 5000) was applied to cut several parallel extruded green microfibers simultaneously under the microscope (Olympus, DSX-1000) to obtain MPs, the cutting edge of blade remains sharp after cutting a thousand times (Supplementary Fig. 11). Afterward, the MPs were aged in the oven at 65 °C for 1.5 h and air-dried on Teflon film at room temperature for 12 h.

MPs sintering

The optimal sintering profiles were designed based on the DTG analysis and previous ceramic sintering studies (Supplementary Fig. 20, Supplementary Table 2). Low heating rate and longtime heat preservation are applied during the period of rapid weight loss or heat flow change. The SiO_2 MP green bodies were heated from room temperature to 705 °C at a rate of 0.5 °C/min, then to 1150 °C at a rate of 1 °C/min. The temperature was kept at 78, 282, 394, 581 °C for 0.5 h, and 705, 1150 °C for 2 h. The Al_2O_3 MP green bodies were heated from room temperature to 632 °C at a rate of 1 °C/min, then to 1550 °C at a rate of 5 °C/min. The temperature was preserved at 147, 316, 365, 561 °C for 0.5 h, and 632, 1550 °C for 2 h. The Si_3N_4 MP green bodies were heated from room temperature to 570 °C at a rate of 1 °C/min, then to 1750 °C at a rate of 5 °C/min. The temperature was preserved for 0.5 h at 86, 163, 352, 522 °C, and 1 h at 570 and 1750 °C, respectively. All the sintering (including debinding) processes were conducted under air atmosphere, and the sintered MPs were finally obtained after the furnace cooling.

Materials characterization

The morphologies of the materials were observed through the stereo microscope (Nikon, SMZ1000), upright optical microscope (Olympus, BX60F5) and scanning electron microscope (FE-SEM, 7600F). The transmittance of various BSs and CS was measured using an ultraviolet-visible spectrophotometer (UV-vis, SHIMADZU, UV-2700) over a wavelength range of 190 – 800 nm. The viscosity and modulus of the samples were measured using a rotational rheometer (Anton Paar, MCR 702e) with steel parallel-plate geometry (Supplementary Table 1, Supplementary Fig. 7). An annular wall sprayed with water covers the experimental set-up peripherally to prevent rapid sample water evaporation during the measuring process. The temperature was increased at 6.49 °C/min. All rheological characterizations were conducted with a preliminary equilibration time of 3 min. The size distribution of ball-milled NPs and zeta-potential of BSs were respectively measured based on dynamic light scattering and phase analysis light scattering using a particle characterization instrument (Brookhaven, NanoBrook 90Plus PALS). FTIR spectra of samples were examined with an attenuated total reflection FTIR (PerkinElmer, Frontier). XPS (Kratos AXIS Supra) with 225W Al Kα radiations was carried out to confirm the sample's composition. SEM-associated energy-dispersive X-ray (EDX) spectroscopy was used to analyze the elements and their distribution in samples. Before SEM and EDX characterization, dried samples were stuck on the sample stage, blown clean and coated with a thin layer of gold on the surface. The coating was conducted in an auto fine coater (JEOL, JFC-1600) for 20 s with 20-mA current intensity. Thermogravimetric analysis (TGA) and differential scanning calorimetry (DSC) were simultaneously conducted under air atmosphere using a thermal analysis instrument (TA, SDT Q600). Temperature of PAM, SiO_2 + PAM, Al_2O_3 + PAM and Si_3N_4 + PAM samples ramped up at 15 °C/min from room temperature to 800, 1200, 1400 and 1400 °C, respectively. The transmission electron microscope (TEM, FEI, Technai F20) was used to test the ceramic structure of the sintered MPs. TEM samples were prepared using the precision ion polishing system (Gatan, PIPS II 695). The sintered MPs were ground to powder and tested by X-ray diffraction (XRD, Bruker, D8 Advance). Atomic force microscope (AFM) images were acquired by an AFM (Park Systems, NX10). Double-sided carbon tape was used to attach the rigid ceramic MPs to the sample stage. The densities of the sintered MPs were measured at room temperature using a densimeter (Alfa Mirage, SD-200L, 0.0001 g/cm^3 resolution) based on Archimedes's principle. The hardness of the substrate was measured using a Vickers hardness tester (WILSON, VH1150). The indenter is a square-based pyramid with the opposite sides meeting at the apex at an angle of 136°. It was pressed into the surface of 7075 Aluminum alloy, T2 copper, PS, PMMA, and wood substrates at loads of 5, 1, 0.5, 1, 0.5 kgf (kilogram-force), respectively. The diagonals of the indentation were measured using a calibrated microscope. The Vickers hardness number (HV) was then calculated based on the formula: $HV = 1.854(F/d^2)$, where F is the applied load in kgf, d is the Arithmetic mean of the two diagonals in millimeters.

Mechanical tests

Compression tests of sintered MPs were performed using a mechanical tester (MTS, C42) with a 250 N load cell (MTS, LSB.252). The top press head went down at a constant speed of 0.1 mm/min. The energy absorption of the MPs was calculated from the area below the force–displacement curve until fracture. For bending tests, a machined steel substrate with a zigzag cross-sectional profile on the top surface is applied as the MP sample holder. The spacing distance between adjacent ridges (or grooves) of the zigzag profile is 0.5 mm. The adjacent two ridges on the top of the substrate act as two supporting pins. A blunted and rounded blade made of SK2 alloy steel was used as the loading pin and installed into the mechanical tester (MTS, C42) with a rigid gripper. It was initially pressed down to a groove between a pair of ridges, during which the position of the substrate on the sample stage was instantly adjusted to ensure the alignment. Afterward, the sample holder was fixed, and the functional supporting ridges were marked. Different square MPs with a length of about 0.8 mm were bridged over the marked supporting pins with the assistance of a portable microscope. Samples with larger dimensions were cast-molded using the same formulas and then cut into bar-shaped green bodies with square cross-sections. The average side lengths of the bar samples after sintered were 2.45, 2.70, and 2.41 mm for SiO_2, Al_2O_3 and Si_3N_4 materials, respectively. The span for testing bar samples was set as 5 mm. The loading rate was set as 0.1 mm/min.

Scratch sample preparation

A piece of glass slide adhered with a layer of double-sided carbon tape (2 × 2mm^2) was utilized as the substrate for the scratch samples preparation. MP was attached to the straight slender beam that was bedewed with DI water. Interfacial tension of the water held the MP immobilized on the beam for about 10 s before the water was fully evaporated, during which the central axis of MP was tuned to be 70° intersecting with the substrate, MP was quickly moved forward and stuck on the surface of tape. The beam was then removed. After drying for about 5 min, a small amount of Cyanoacrylate glue (ergo, 5800, Switzerland) was poured around the MP and immersed the bottom of MP. The scratch sample preparation was finally completed after drying overnight.

Scratch test

The substrate of the scratch sample was attached to the center of the top press head upside down using cyanoacrylate glue. The test substrate was placed beneath the MP. The top press head was moved forward until the pressure reached a certain value (1.5, 9, 13, 1, 6 and 9 N for T-SiO_2, T-Al_2O_3, T-Si_3N_4, S-SiO_2, S-Al_2O_3 and S-Si_3N_4 MPs, respectively), and then the test substrate was dragged out at a constant speed along a ruler fixed beside. Scratches were characterized and analyzed using a digital microscope (Olympus, DSX-1000). The half-embedded

https://doi.org/10.1038/s41467-024-53016-8

MPs were released using adhesive remover (ergo, 9153, Switzerland) for further characterization.

Statistical analysis

Excel and Origin 2022 were used to analyze and plot the data. Image J was used for image analysis and measurement. Solidworks 2020 was used to do the schematic illustration and the modeling of MC transformations. XPS profiles were analyzed by ESCApe software system. Jade 6.5 was used to analyze the XRD result.

Data availability

All data needed to evaluate the conclusions in the paper are available in this Article or its Supplementary information. The data generated in this study are provided in the Source Data file. Source data are provided with this paper. Additional data are available from authors upon request. Source data are provided with this paper.

References

1. Wang, S. et al. Skin electronics from scalable fabrication of an intrinsically stretchable transistor array. *Nature* **555**, 83–88 (2018).
2. Zhang, Z. et al. High-brightness all-polymer stretchable LED with charge-trapping dilution. *Nature* **603**, 624–630 (2022).
3. Joh, H. & Fan, D. E. Materials and schemes of multimodal reconfigurable micro/nanomachines and robots: review and perspective. *Adv. Mater.* **33**, 2101965 (2021).
4. Halder, A. & Sun, Y. Biocompatible propulsion for biomedical micro/nano robotics. *Biosens. Bioelectron.* **139**, 111334 (2019).
5. Randall, C. L., Gultepe, E. & Gracias, D. H. Self-folding devices and materials for biomedical applications. *Trends Biotechnol.* **30**, 138–146 (2012).
6. Shakoor, A., Gao, W., Zhao, L., Jiang, Z. & Sun, D. Advanced tools and methods for single-cell surgery. *Microsyst. Nanoeng.* **8**, 47 (2022).
7. Chen, H., Zhou, C., Li, Y., Liang, S. & Li, J. Dielectric tetrahedrons as terahertz resonators switched from perfect absorber to reflector. *Sci. Rep.* **10**, 17134 (2020).
8. Zhou, C., Liang, S., Li, Y., Li, J. & Chen, H. Microfluidic assembly of micro-blocks into interlocked structures for enhanced strength and toughness. *ACS Appl. Mater. Interfaces* **14**, 7261–7269 (2022).
9. Shepherd, R. F. et al. Stop-flow lithography of colloidal, glass, and silicon microcomponents. *Adv. Mater.* **20**, 4734–4739 (2008).
10. Wang, S.-H., Wang, P.-H., Hsieh, I.-M. & Hsieh, C.-C. Microfluidic synthesis of silica microcomponents using sol-gel process and stop-flow lithography. *J. Taiwan Inst. Chem. Eng.* **93**, 103–108 (2018).
11. Oliaei, S. N. B., Karpat, Y., Paulo Davim, J. & Perveen, A. Micro tool design and fabrication: a review. *J. Manuf. Process.* **36**, 496–519 (2018).
12. O'Hara, J. & Fang, F. Z. Advances in micro cutting tool design and fabrication. *Int. J. Extrem. Manuf.* **1**, 032003 (2019).
13. Gao, S. & Huang, H. Recent advances in micro- and nano-machining technologies. *Front. Mech. Eng.* **12**, 18–32 (2017).
14. King, P. C., Zahiri, S. H. & Jahedi, M. Focused ion beam micro-dissection of cold-sprayed particles. *Acta Mater.* **56**, 5617–5626 (2008).
15. Palima, D. & Glückstad, J. Gearing up for optical microrobotics: micromanipulation and actuation of synthetic microstructures by optical forces. *Laser Photon. Rev.* **7**, 478–494 (2013).
16. Boswell, B., Islam, M. N. & Davies, I. J. A review of micro-mechanical cutting. *Int. J. Adv. Manuf. Technol.* **94**, 789–806 (2018).
17. Ge, Q. et al. Projection micro stereolithography based 3D printing and its applications. *Int. J. Extreme Manuf.* **2**, 022004 (2020).
18. Dendukuri, D. & Doyle, P. S. The synthesis and assembly of polymeric microparticles using microfluidics. *Adv. Mater.* **21**, 4071–4086 (2009).
19. Jo, Y. K. & Lee, D. Biopolymer microparticles prepared by microfluidics for biomedical applications. *Small* **16**, 1903736 (2020).
20. Zhou, C., Liang, S., Li, Y., Chen, H. & Li, J. Fabrication of sharp-edged 3D microparticles via folded PDMS microfluidic channels. *Lab Chip* **22**, 148–155 (2021).
21. Zhou, C. et al. Tailoring 3D shapes of polyhedral microparticles by adjusting orthogonal projection in a microfluidic channel. *J. Polym. Sci.* **60**, 1750–1757 (2022).
22. Zhou, C. et al. Fabrication of crescent-shaped ceramic microparticles based on single emulsion microfluidics. *Ceram. Int.* **47**, 10866–10872 (2021).
23. Zhou, C. et al. Double UV lights intersection shaping for bowl-shaped ceramic microparticles based on microfluidics. *Ceram. Int.* **48**, 27590–27596 (2022).
24. Paulsen, K. S., Di Carlo, D. & Chung, A. J. Optofluidic fabrication for 3D-shaped particles. *Nat. Commun.* **6**, 6976 (2015).
25. Paulsen, K. S., Deng, Y. & Chung, A. J. DIY 3D microparticle generation from next generation optofluidic fabrication. *Adv. Sci.* **5**, 1800252 (2018).
26. Chung, S. E., Park, W., Shin, S., Lee, S. A. & Kwon, S. Guided and fluidic self-assembly of microstructures using railed microfluidic channels. *Nat. Mater.* **7**, 581–587 (2008).
27. Yuan, R. et al. Designable 3D microshapes fabricated at the intersection of structured flow and optical fields. *Small* **14**, 1803585 (2018).
28. Chen, L. et al. Flexible octopus-shaped hydrogel particles for specific cell capture. *Small* **12**, 2001–2008 (2016).
29. Pregibon, D. C., Toner, M. & Doyle, P. S. Multifunctional encoded particles for high-throughput biomolecule analysis. *Science* **315**, 1393–1396 (2007).
30. Lee, H., Kim, J., Kim, H., Kim, J. & Kwon, S. Colour-barcoded magnetic microparticles for multiplexed bioassays. *Nat. Mater.* **9**, 745–749 (2010).
31. Han, S. et al. Lithographically encoded polymer microtaggant using high-capacity and error-correctable QR code for anti-counterfeiting of drugs. *Adv. Mater.* **24**, 5924–5929 (2012).
32. Rehor, I. et al. Biodegradable microparticles for simultaneous detection of counterfeit and deteriorated edible products. *Small* **13**, 1701804 (2017).
33. Lee, J. et al. Universal process-inert encoding architecture for polymer microparticles. *Nat. Mater.* **13**, 524–529 (2014).
34. Zhou, C., Cao, Y., Liu, C. & Guo, W. Microparticles by microfluidic lithography. *Mater. Today* **67**, 178–202 (2023).
35. Decker, C. & Jenkins, A. D. Kinetic approach of oxygen inhibition in ultraviolet-and laser-induced polymerizations. *Macromolecules* **18**, 1241–1244 (1985).
36. Dendukuri, D., Pregibon, D. C., Collins, J., Hatton, T. A. & Doyle, P. S. Continuous-flow lithography for high-throughput microparticle synthesis. *Nat. Mater.* **5**, 365–369 (2006).
37. Hakimi, N., Tsai, S. S. H., Cheng, C.-H. & Hwang, D. K. One-step two-dimensional microfluidics-based synthesis of three-dimensional particles. *Adv. Mater.* **26**, 1393–1398 (2013).
38. Heinze, M. Wear resistance of hard coatings in plastics processing. *Surf. Coat. Technol.* **105**, 38–44 (1998).
39. Silva, F. J. G., Martinho, R. P., Alexandre, R. J. D. & Baptista, A. P. M. Increasing the wear resistance of molds for injection of glass fiber reinforced plastics. *Wear* **271**, 2494–2499 (2011).
40. Buchwalter, S. L. *Encyclopedia of Materials: Science and Technology* (Elsevier, 2001).
41. Xie, R. et al. Glass transition temperature from the chemical structure of conjugated polymers. *Nat. Commun.* **11**, 893 (2020).
42. Kitahara, Y. et al. Thermal decomposition of acrylamide from polyacrylamide. *J. Therm. Anal. Calorim.* **110**, 423–429 (2012).

43. Fox, D. S., Opila, E. J., Nguyen, Q. N., Humphrey, D. L. & Lewton, S. M. Paralinear oxidation of silicon nitride in a water-vapor/oxygen environment. *J. Am. Ceram. Soc.* **86**, 1256–1261 (2003).
44. Qadir, A., Fogarassy, Z., Horváth, Z. E., Balazsi, K. & Balazsi, C. Effect of the oxidization of Si_3N_4 powder on the microstructural and mechanical properties of hot isostatic pressed silicon nitride. *Ceram. Int.* **44**, 14601–14609 (2018).
45. Loehman, R. E. & Rowcliffe, D. J. Sintering of Si_3N_4-Y_2O_3-Al_2O_3. *J. Am. Ceram. Soc.* **63**, 144–148 (1980).
46. Ceja-Cárdenas, L., Lemus-Ruíz, J., Jaramillo-Vigueras, D. & de la Torre, S. D. Spark plasma sintering of α-Si_3N_4 ceramics with Al_2O_3 and Y_2O_3 as additives and its morphology transformation. *J. Alloy. Compd.* **501**, 345–351 (2010).
47. Wang, L., Tien, T. Y. & Chen, I. W. Formation of β-silicon nitride crystals from (Si, Al, Mg, Y)(O, N) liquid: I, phase, composition, and shape evolutions. *J. Am. Ceram. Soc.* **86**, 1578–1585 (2003).
48. Shen, Z., Zhao, Z., Peng, H. & Nygren, M. Formation of tough interlocking microstructures in silicon nitride ceramics by dynamic ripening. *Nature* **417**, 266–269 (2002).
49. Perera, D. S., Mitchell, D. R. G. & Leung, S. High aspect ratio β-Si_3N_4 grain growth. *J. Eur. Ceram. Soc.* **20**, 789–794 (2000).
50. Huang, Z. K., Greil, P. & Petzow, G. Formation of silicon oxinitride from Si_3N_4 and SiO_2 in the presence of Al_2O_3. *Ceram. Int.* **10**, 14–17 (1984).
51. Bergman, B. & Heping, H. The influence of different oxides on the formation of Si_2N_2O from SiO_2 and Si_3N_4. *J. Eur. Ceram. Soc.* **6**, 3–8 (1990).
52. Baah, D., Donnell, T., Tigner, J. & Floyd-Smith, T. Stop flow lithography synthesis of non-spherical metal oxide particles. *Particuology* **14**, 91–97 (2014).
53. Jia, Y., Kanno, Y. & Xie, Z. New gel-casting process for alumina ceramics based on gelation of alginate. *J. Eur. Ceram. Soc.* **22**, 1911–1916 (2002).
54. Jia, Y., Kanno, Y. & Xie, Z. Fabrication of alumina green body through gelcasting process using alginate. *Mater. Lett.* **57**, 2530–2534 (2003).
55. Xie, R., Zhang, D., Zhang, X., Zhou, K. & Button, T. W. Gelcasting of alumina ceramics with improved green strength. *Ceram. Int.* **38**, 6923–6926 (2012).
56. Bocanegra-Bernal, M. H. & Matovic, B. Dense and near-net-shape fabrication of Si_3N_4 ceramics. *Mater. Sci. Eng. A* **500**, 130–149 (2009).
57. Yang, X. et al. Fabrication and properties of porous silicon nitride wave-transparent ceramics via gel-casting and pressureless sintering. *Mater. Sci. Eng. A* **663**, 174–180 (2016).
58. Zou, C., Zhang, C., Li, B., Wang, S. & Cao, F. Microstructure and properties of porous silicon nitride ceramics prepared by gel-casting and gas pressure sintering. *Mater. Des.* **44**, 114–118 (2013).
59. Li, W., Chen, P., Gu, M. & Jin, Y. Effect of TMAH on rheological behavior of SiC aqueous suspension. *J. Eur. Ceram. Soc.* **24**, 3679–3684 (2004).
60. Zhang, J. et al. Effect of TMAH on the rheological behavior of alumina slurries for gelcasting. *J. Asian Ceram. Soc.* **5**, 261–265 (2017).

Acknowledgements
We thank J.C., T.S., Y.L., D.A., W.L., Z.G., S.T., and Y.S. for the technical support. We also appreciate the valuable discussion with Y.T. and Y. C. This study received funding support from the Ministry of Education in Singapore under grant MOE-MOET32022-0002 (N.-J.C.) and the National Natural Science Foundation of China under grants No. 51905033 (S.L.) and 52105193 (C.L.).

Author contributions
C.Z. conceived the idea and designed the project under the supervision of N.-J.C. C.Z., S.L., B.Q., and C.L. prepared the devices and precursor solutions, fabricated and characterized the microparticles, and analyzed and discussed the experimental data. C.Z. and N.-J.C. wrote the manuscript with input from all the authors.

Competing interests
The authors declare no competing interests.

Additional information
Supplementary information The online version contains supplementary material available at https://doi.org/10.1038/s41467-024-53016-8.

Correspondence and requests for materials should be addressed to Nam-Joon Cho.

Peer review information *Nature Communications* thanks Jong Wan Ko and Amir Hadian for their contribution to the peer review of this work. A peer review file is available.